Available online at www.sciencedirect.com

SCIENCE DIRECT

Biomaterials 24 (2003) 2673–2683

Biomaterials

www.elsevier.com/locate/biomaterials

Fatigue performance and cyto-toxicity of low rigidity titanium alloy, Ti–29Nb–13Ta–4.6Zr

Mitsuo Niinomi*

Department of Production Systems Engineering, Toyohashi University of Technology, 1-1, Hibarigaoka, Tempaku-cho, Toyohashi 441-8580, Japan

Received 4 June 2002; accepted 23 January 2003

Abstract

A β type titanium alloy, Ti–29Nb–13Ta–4.6Zr, was newly designed and developed for biomedical applications. The new alloy contains non-toxic elements such as Nb, Ta, and Zr. In the present study, phases that appeared in the new alloy through various aging treatments were characterized by hardness tests and microstructural observations in order to identify the phase transformation. Fatigue properties of the new alloy were investigated. Young's modulus and cyto-toxicity of the new alloy were also evaluated.

Precipitated phases distribute homogeneously over the whole specimen, and they are α phase, a small amount of ω phase, and β phase when the new alloys are subjected to aging treatment at 673 K for 259.2 ks after solution treatment at 1063 K for 3.6 ks. The fatigue strength of the new alloy subjected to aging at 673 K for 259.2 ks after solution treatment at 1063 K for 3.6 ks is much better than when subjected to other aging treatments. In this case, the fatigue limit is around 700 MPa. Young's modulus of the new alloy is much smaller than that of Ti–6Al–4V ELI. The cyto-toxicity of the new alloy is equivalent to that of pure Ti. Therefore, it is proposed that the new alloy, Ti–29Nb–13Ta–4.6Zr, will be of considerable use in biomedical applications.

Keywords: Beta titanium alloy; Ti–29Nb–13Ta–4.6Zr; Biomedical application; Low rigidity; Fatigue; Cyto-toxicity

1. Introduction

Pure titanium and $\alpha+\beta$ type Ti–6Al–4V ELI alloys are currently widely used as structural biomaterials for the replacement of hard tissues in devices such as artificial hip joints and dental implants, because they have excellent specific strength and corrosion resistance, and the best biocompatibility characteristics among metallic biomaterials. They are used more than any other titanium biomaterials. However, other new titanium alloys for biomedical applications have now been included in ASTM standardizations. For example, β type Ti–15Mo [1] have been registered in ASTM standardizations, and β type Ti–35Nb–7Zr–5Ta [2], and $\alpha+\beta$ type Ti–3Al–2.5V [3] are in the process of being registered. β type titanium alloys have been developed in order to obtain low rigidity, which is considered effective for promoting bone healing and remodeling. The rigidity of $\alpha+\beta$ type titanium alloys is still considerably greater than that of the cortical bone although the rigidity of titanium alloys is less than that of Co-Cr type alloys and stainless steels used for biomedical applications [4]. The recent trend in research and development of titanium alloys for biomedical applications is to develop low rigidity β type titanium alloys composed of non-toxic and non-allergic elements with excellent mechanical properties and workability [5].

According to this concept, the authors have developed a new β type Ti–29Nb–13Ta–4.6Zr [6–9] alloy composed of elements like Nb, Ta, and Zr [10,11] for biomedical applications. It is still necessary to evaluate various performances of Ti–29Nb–13Ta–4.6Zr for practical use. Fatigue performance is one of the most important mechanical performances for biomaterials because, in general, biomaterials are used under cyclic loading. Fatigue performance of titanium alloy varies according to the change in microstructures by heat treatments.

Fatigue characteristics of the new β type titanium alloy, Ti–29Nb–13Ta–4.6Zr, subjected to various heat treatments were investigated in relation with

*Corresponding author. Tel.: +81-532-44-6706; fax: +81-532-44-6690.

E-mail address: niinomi@sp-mac4.tutpse.tut.ac.jp (M. Niinomi).

0142-9612/03/$ - see front matter
doi:10.1016/S0142-9612(03)00069-3

microstructures in this study. Young's modulus and cyto-toxicity of Ti–29Nb–13Ta–4.6Zr were also evaluated.

2. Experimental procedures

2.1. Material and heat treatment

The main materials used in this study were forged bars of Ti–29Nb–13Ta–4.6Zr (Nb: 31.5, Ta: 11.6, Zr: 4.7, Fe: 0.03, Al: <0.02, C: 0.02, N: 0.03, O: 0.14, H: <0.02, bal: Ti, mass%) with a diameter of 20 mm. They were cold rolled to the plates with a thickness of 2.5 mm.

Some of the cold rolled plates were subjected to solution treatment (ST) at 1063 K for 3.6 ks (ks = 10^3 s) in Ar gas atmosphere followed by water quenching (WQ). The plates subjected to ST were then aged at different temperatures 573, 598 and 673 K, for 259.2 ks in Ar gas atmosphere followed by WQ. This heat treatment process is schematically shown in Fig. 1. As-solution treated alloy and aged alloy after solution treatment (STA) are designated as ST alloy and STA alloy, respectively, hereafter.

For the comparison of cyto-toxicity, commercial pure Ti and Ti–6Al–4V were also used in this study. Pure Ti was annealed at 973 K followed by air cooling. Ti–6Al–4V was annealed at 978 K followed by air cooling.

2.2. Tensile and fatigue tests

Smooth plate specimens, with a rectangular cross section of 3.0 mm × 1.5 mm and a gage length of 13 mm for tensile and fatigue tests were machined from the heat-treated plates with their longitudinal directions parallel to the rolling direction. The geometry of tensile and fatigue test specimen is shown in Fig. 2(a). The machined specimens were wet polished using a #1500 waterproof emery paper and buff polished to produce mirror surfaces.

Tensile tests were carried out on the specimens finished as stated above using an Instron-type machine with a crosshead speed of 8.33×10^{-6} m/s in air at 295 K. The strain was measured using a clip gage attached to the gage length area of the specimen and a foil strain gage attached directly to the gage section of the specimen.

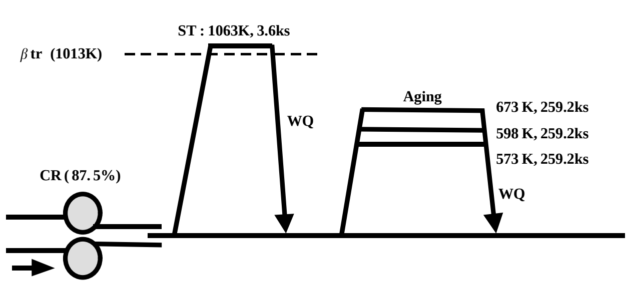

Fig. 1. Schematic drawing of thermomechanical processing for Ti–29Nb–13Ta–4.6Zr. CR, ST and WQ indicate cold rolling, solutionizing and water quenching.

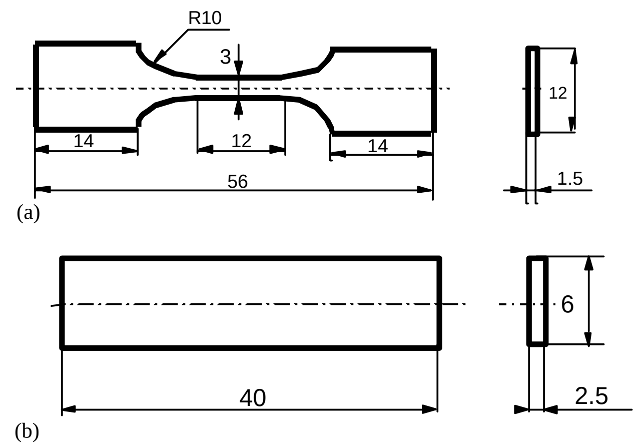

Fig. 2. Geometries of specimen for tensile and fatigue tests, and measuring Young's modulus.

Fatigue tests were carried out on the specimens finished as stated above using an electro-servo-hydraulic fatigue testing machine. Each fatigue testing was performed at a frequency of 10 Hz with a stress ratio, $R = 0.1$, under a tension–tension stress mode in air at 295 K.

2.3. Measurement of Young's modulus

Specimens for measuring Young's modulus with a size of 40 mm × 6 mm × 2.5 mm, as shown in Fig. 2(b), were also machined according to the same procedure as those of machining tensile and fatigue test specimens. Specimens for measuring Young's modulus were finally wet polished using a #1500 waterproof emery paper. Young's modulus was measured using a piezoelectric composite method [12] in air at 295 K.

2.4. Evaluation of aging behavior

Blocks with a length of 3 mm, a width of 3 mm, and thickness of 3 mm were mechanically cut from the present alloy. The blocks were subjected to ST at 1063 K for 3.6 ks followed by WQ. After ST, the blocks were aged at 573, 593 and 673 K, respectively, for different times. After these various aging treatments, the Vickers hardness of each aged specimen was measured with a load of 98 N and a holding time of 10 s using a Vickers hardness tester. Then the age hardening curve at each aging temperature was made. These methods are schematically shown in Fig. 3.

2.5. Characterization of precipitated phase

Characterization of the precipitated phase was carried out using a scanning electron microscope (SEM), a

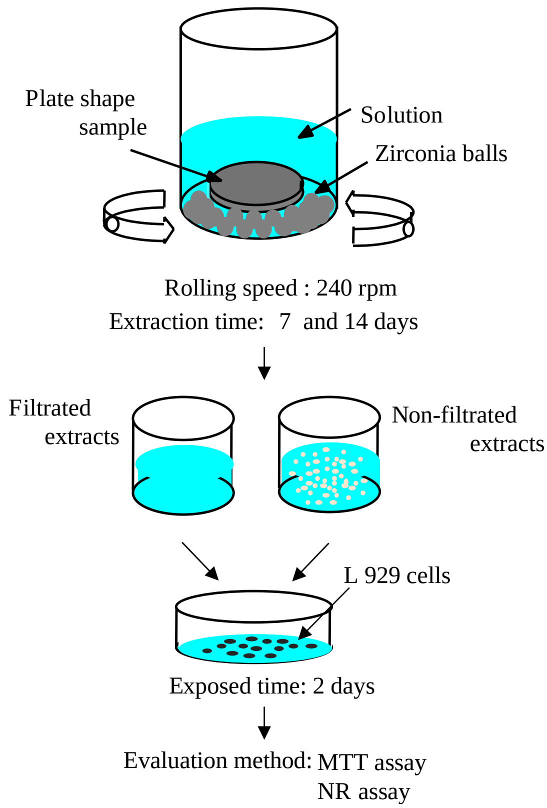

Fig. 3. Schematic explanation of evaluation method of cell viability.

transmission electron microscope (TEM), and X-ray analysis.

For SEM observation, block specimens with a size of 3 mm × 3 mm × 3 mm were machined from variously heat-treated alloys. Each specimen was mirror finished by buff polishing after being polished using a #1500 waterproof emery paper. After mirror finishing, each specimen was etched by (2% HF + 5% H_2NO_3) solution. Then each specimen was characterized using an SEM.

For TEM observation, disk specimens with a diameter of 2.9 mm and a thickness of 0.5 mm were machined from variously heat-treated alloys, and electro polished to make thin foil. TEM observation was carried out on the thin foil with an accelerating voltage of 200 kV.

X-ray diffraction analysis was carried out on the same specimens used for SEM observations using a Cu target with an accelerating voltage of 40 kV and a current of 30 mA.

2.6. Evaluation of cyto-toxicity

Biocompatibility of Ti–29Nb–13Ta–4.6Zr, pure Ti and Ti–6Al–4V was judged by evaluating the cyto-toxicity. Plate specimens with a size of 25 mm × 25 mm × 2 mm were machined from each alloy, and then polished using a #1200 water proof emery paper. Each plate specimen was put on zirconia balls in a vessel, and in the autoclave. The vessel with 10 ml Eagle's culture solution at a temperature of 310 K was rotated with a speed of 240 rpm, and extraction periods were 7 and 14 days. As-extracted solution and filtrated extract solution using a 0.22 μm membrane filter were prepared. In the As-extracted solution and filtrated extracted solution, the survival rate of L929 cells derived from mice was evaluated using the NR [13] and MTT [14] methods. The exposure period of L929 cells to extract solutions was 2 days. The MTT method is a method for evaluating the cell respiration by the mitochondria, while the NR method is a method for evaluating the ratio of sound cells of which cell membranes have no lesion by the amount of Neutral Red (NR) pigment. The survival rate of L929 cells indicates the cyto-toxicity level of the extracts.

3. Results and discussion

3.1. Aging behavior

Fig. 4 shows the age hardening curve of the present alloy aged at 573, 598 or 673 K after ST at 1063 K for 3.6 ks. The data As-ST indicates the hardness of the present alloy in As-solutionized conditions, and the value is Hv 175. For every aging temperature, the Vickers hardness increases gradually up to an aging time of 10.8 ks (the first aging step), and increases rapidly from an aging time of 10.8 ks to an aging time of 172.8 ks (the second aging step). An increasing ratio of Vickers hardness per one ks for an aging temperature

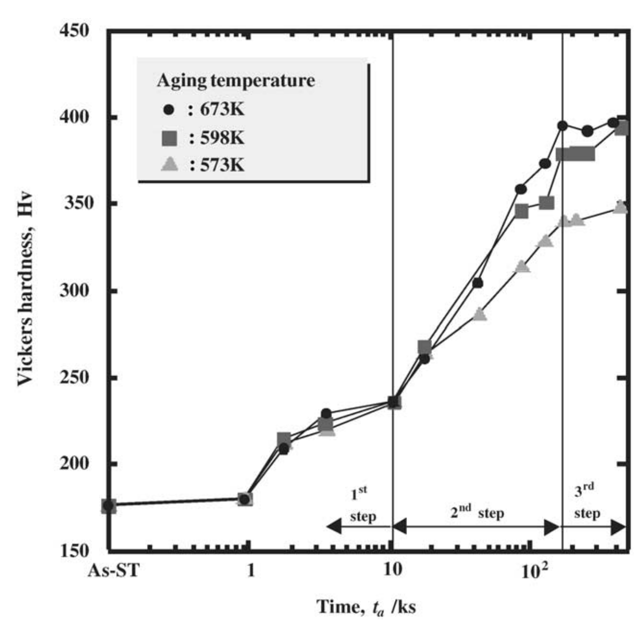

Fig. 4. Aging curves of Ti–29Nb–13Ta–4.6Zr aged at 573, 598 and 673 K, respectively, after ST.

of 673 K in the second aging step is around Hv 1.27, which is relatively greater than that for other aging temperatures. For every aging temperature, the Vickers hardness becomes constant after 172.8 ks. Finally the aging curve shows a three-step hardening behavior.

Focusing on the second aging step region where the Vickers hardness increases rapidly for every aging temperature, hardness up to an aging time of 43.2 ks is the greatest in the alloy aged at 598 K, but the hardness after a aging time of 86.4 ks is the greatest in the alloy aged at 673 K. This phenomenon is considered due to the difference in the volume fraction of precipitated α phase or ω phase.

In this study, an aging time of 259.2 ks for each aging temperature of 573, 598 or 673 K was selected for the aging treatment of tensile and fatigue test specimens considering the practical heat treatment processing, although the alloy is not in the peak aged condition at each aging temperature. At this aging time, the Vickers hardness of the alloy aged at 573, 598 and 673 K are Hv 345, Hv 370 and Hv 395, respectively. Therefore, relatively excellent mechanical properties are expected in the aging treatments in this study.

3.2. Microstructure

Microstructures of Ti–29Nb–13Ta–4.6Zr subjected to various heat treatments are shown in Fig. 5. Ti–29Nb–13Ta–4.6Zr subjected to ST has only the α phase with an average diameter of 20 μm (Fig. 5(a)). In Ti–29Nb–13Ta–4.6Zr aged at temperatures between 573 K and 673 K after ST, it is difficult to observe precipitated phases as shown in Fig. 5(b)–(d) although fine α phases or ω phase is considered to exist in β grains. It is also difficult to identify these precipitated phases clearly by SEM.

X-ray diffraction profiles of ST and STA alloys are shown in Fig. 6. In ST alloy, only α phase peaks are detected. In every STA alloy, ω phase peaks are detected in addition to β phase peaks. The peak of ω phase is the greatest in the alloy aged at 598 K, but very low in the alloy aged at 673 K. In the alloy aged at 673 K, α phase peaks are detected in addition to the β and ω phase peaks. α phase precipitation is therefore one of the main causes for the greatest increasing rate of Vickers

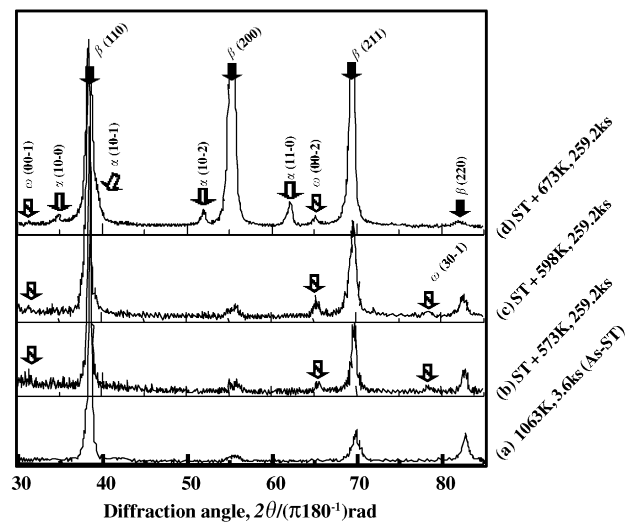

Fig. 6. X-ray diffraction profile of Ti–29Nb–13Ta–4.6Zr subjected to each heat treatment.

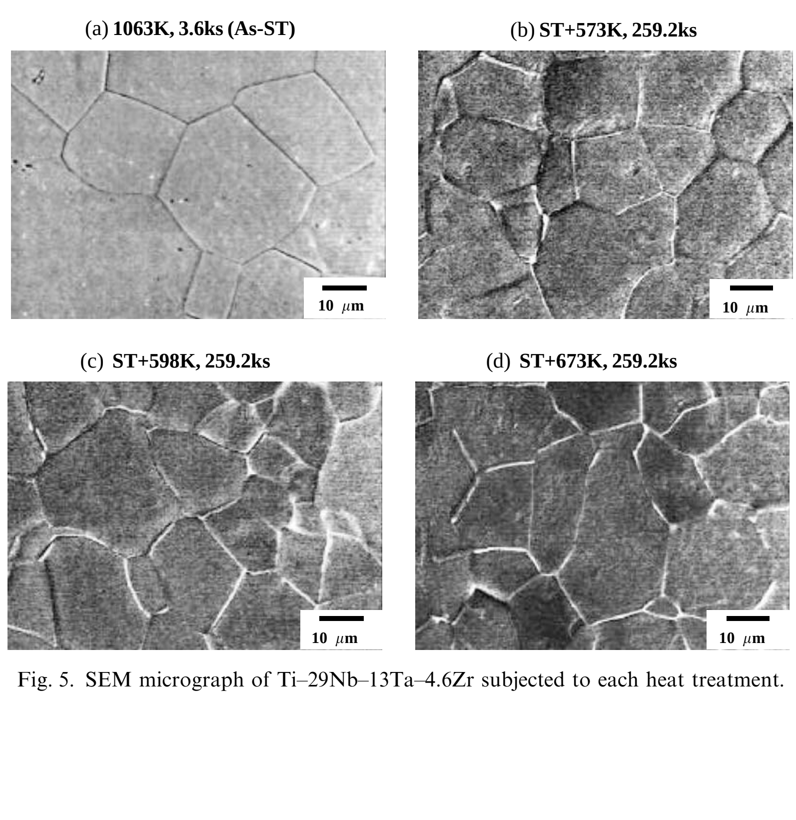

Fig. 5. SEM micrograph of Ti–29Nb–13Ta–4.6Zr subjected to each heat treatment.

hardness at an aging temperature of 673 K in the second aging step as previously stated in Section 3.1.

Fig. 7 shows the TEM microstructure and diffraction pattern of ST alloy. No precipitated α and ω phases are observed in TEM microstructure of ST alloy, which is consistent with the result of X-ray analysis shown above. The diffraction pattern of ST alloy shows the diffraction spots to be consistent with those of {1 1 1} of body centered structure (bcc). Those results confirm that ST alloy is composed of single β phase.

Fig. 8 shows TEM microstructure and diffraction pattern of STA alloy aged at 673 K, representatively. Very fine precipitates with two variants at least are distributed homogeneously in β phase. Two types of morphologies of precipitates are observed, bar type and acicular type, with a length of around 100 nm. As a result of structural analysis on acicular type precipitates, the diffraction pattern was found to be consistent with that of {2 1 1 0} of α phase of pure Ti. Therefore, the acicular type precipitates were recognized as α phase. The bar type precipitates are not identified, but they are considered to be α phase similar to the acicular type precipitates identified as α phases, as stated above. In this case, very weak diffractions from (1 0 1 1) of ω phases are observed as shown in Fig. 9 confirming the existence of ω phases. It is therefore difficult to recognize the existence of ω phases in bright field image because precipitated ω phases in β type titanium alloys are generally very fine (around 10 nm) [15], and in addition, the volume fraction of ω phases is very small because most of the ω phases transform to α phases.

3.3. Tensile properties

Tensile strength, 0.2% proof stress, and elongation of ST and STA alloy are shown in Fig. 10. The tensile strength, 0.2% proof stress and elongation of ST alloy are around 650 MPa, 600 MPa and 25%, respectively.

The tensile strength and 0.2% proof stress of each STA alloy increases with increase in aging temperature. The tensile strength and 0.2% stress of around 1050 and 1000 MPa, respectively, in STA alloy aged at 598 K are the greatest among other STA alloys, although elongation of around 5% is the smallest. The tensile strength and 0.2% proof stress of STA alloy aged at 673 K are a little smaller than those of STA alloy aged at 598 K, but elongation tends to recover around 15%. Since α phases precipitate in addition to the precipitation of ω phases, which lead to brittle fracture, and according to the α phase precipitation, the volume fraction of ω phases decreases in STA alloy aged at 673 K, the recovery of

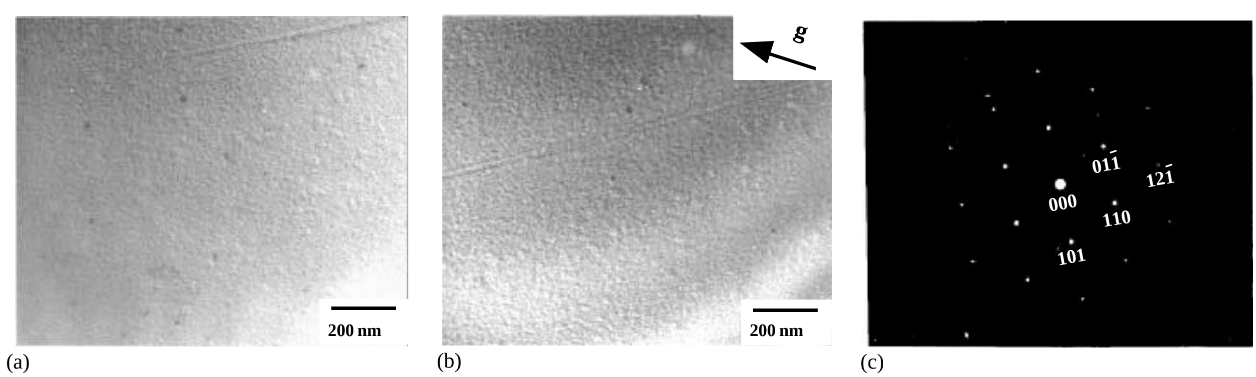

Fig. 7. TEM micrographs and diffraction pattern of Ti–29Nb–13Ta–4.6Zr subjected to ST at 1063 K for 3.6 ks: (a) bright field image, (b) dark field image, and (c) diffraction pattern.

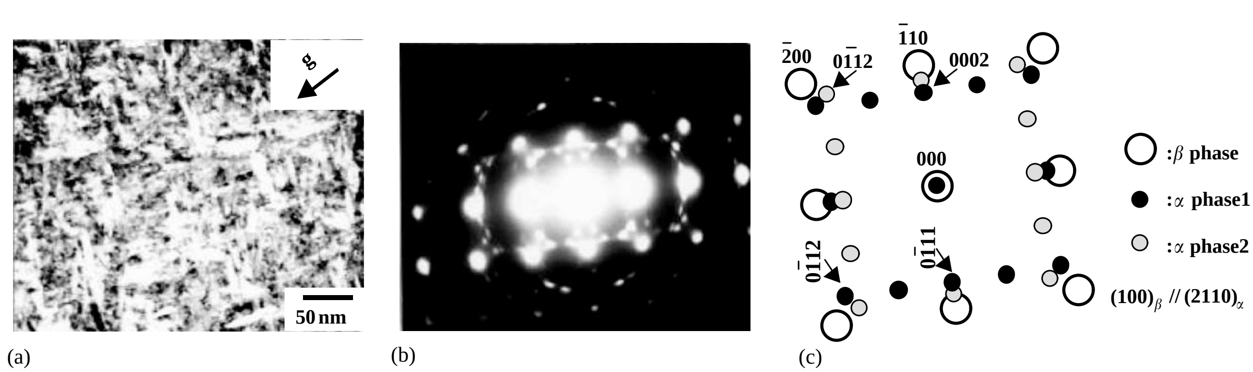

Fig. 8. Transmission electron micrograph, diffraction pattern and key diagram of Ti–29Nb–13Ta–4.6Zr aged at 673 K for 259.2 ks after ST at 1063 K for 3.6 ks: (a) dark field image of a phase, (b) diffraction pattern, and (c) key diagram.

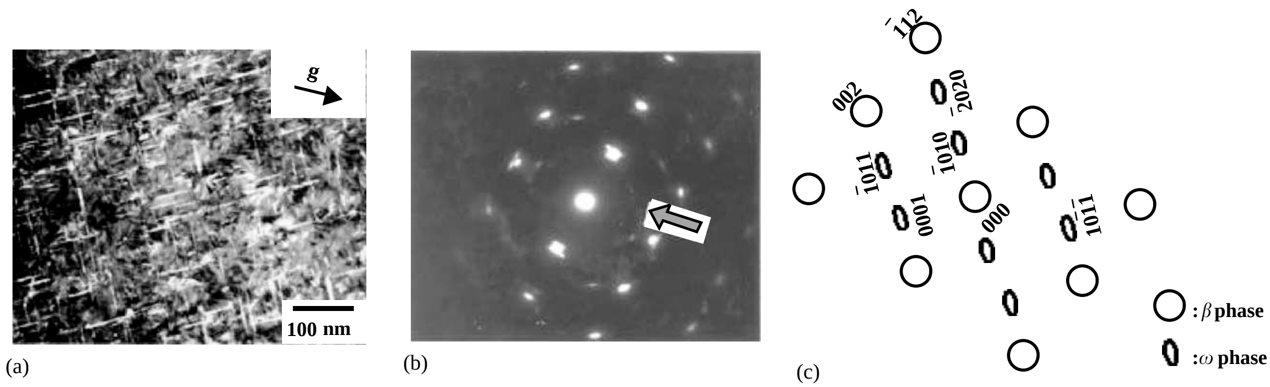

Fig. 9. Transmission electron micrograph, diffraction pattern and key diagram of Ti–29Nb–13Ta–4.6Zr aged at 673 K for 259.2 ks after ST at 1063 K for 3.6 ks. Arrow shows ω phase spot: (a) dark field image of ω phase, (b) diffraction pattern, and (c) key diagram.

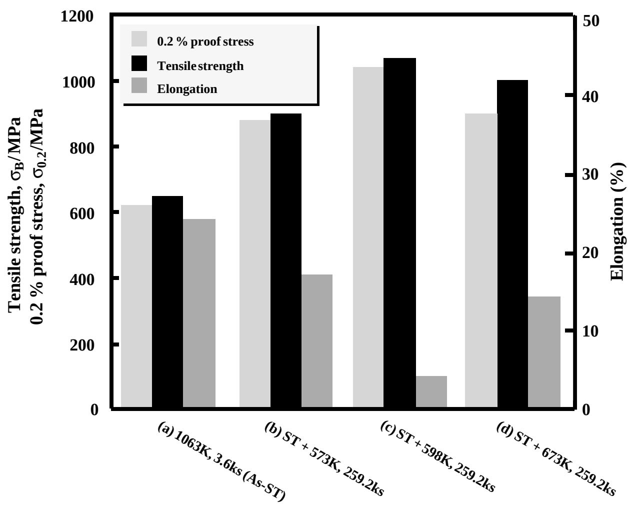

Fig. 10. Tensile properties of Ti–29Nb–13Ta–4.6Zr subjected to each heat treatment.

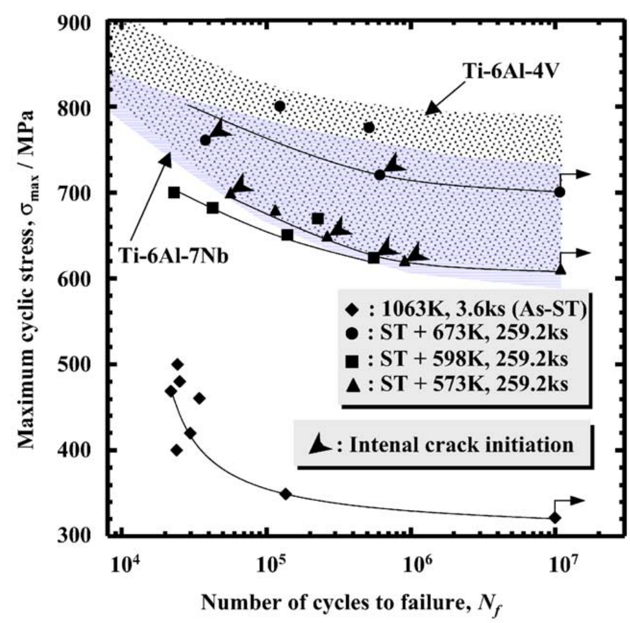

Fig. 11. S–N curve of Ti–29Nb–13Ta–4.6Zr subjected to each heat treatment and range of S–N data of Ti–6Al–4V and Ti–6Al–7Nb.

elongation is considered to occur. As a result, Ti–29Nb–13Ta–4.6Zr aged at 673 K after ST has a relatively excellent balance of strength and elongation.

3.4. Fatigue strength and fatigue fracture surface morphology

The S–N curves, obtained from plain fatigue tests on ST and STA alloys are shown in Fig. 11. The ranges of fatigue strength of conventional biomedical Ti–6Al–4V ELI and Ti–6Al–7Nb obtained from the literatures [16–18], are also shown in the same figure for comparison. The maximum stress, at which the specimen has not failed at 10^7 cycles, is defined as a fatigue limit in this study. V marks added to the data points in Fig. 9 indicate the subsurface crack initiations. For the other data without V marks, the crack initiates from the surface of the specimen.

The fatigue strength of ST alloy is the lowest in both low cycle fatigue life region where the number of cycles to failure is less than 10^4 cycles and high cycle fatigue life region where the number of cycles to failure is over 10^5 cycles. The fatigue limit of ST alloy is around 320 MPa.

On the other hand, the fatigue strength of each STA alloy is similar to that of Ti–6Al–4V ELI and Ti–6Al–7Nb, and is around two times greater than that of ST alloy. The fatigue limit of STA alloy aged at 673 K is around 700 MPa, which is the greatest and nearly the upper limit of fatigue limit of Ti–6Al–4V ELI. This is due to the improvement of the balance of strength and ductility brought by the precipitation of α phases and a small amount of ω phases, which leads to increase the resistance to the fatigue crack initiation and small fatigue crack propagation.

Fig. 12 shows SEM fractographs of ST alloy in low and high cycle fatigue life regions. Fatigue crack initiates from the surface of the specimen and then propagates parabolically towards the inside of the specimen in every

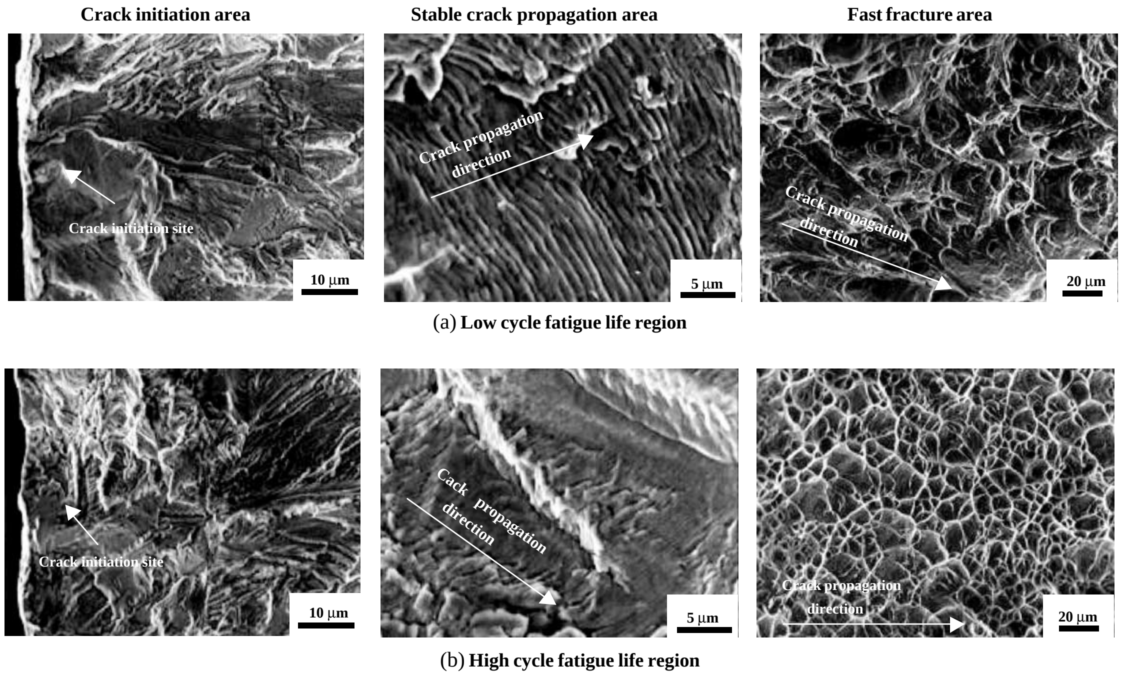

Fig. 12. SEM fractographs of as-solutionized Ti–29Nb–13Ta–4.6Zr tested in (a) low cycle fatigue life region and (b) high cycle fatigue life region.

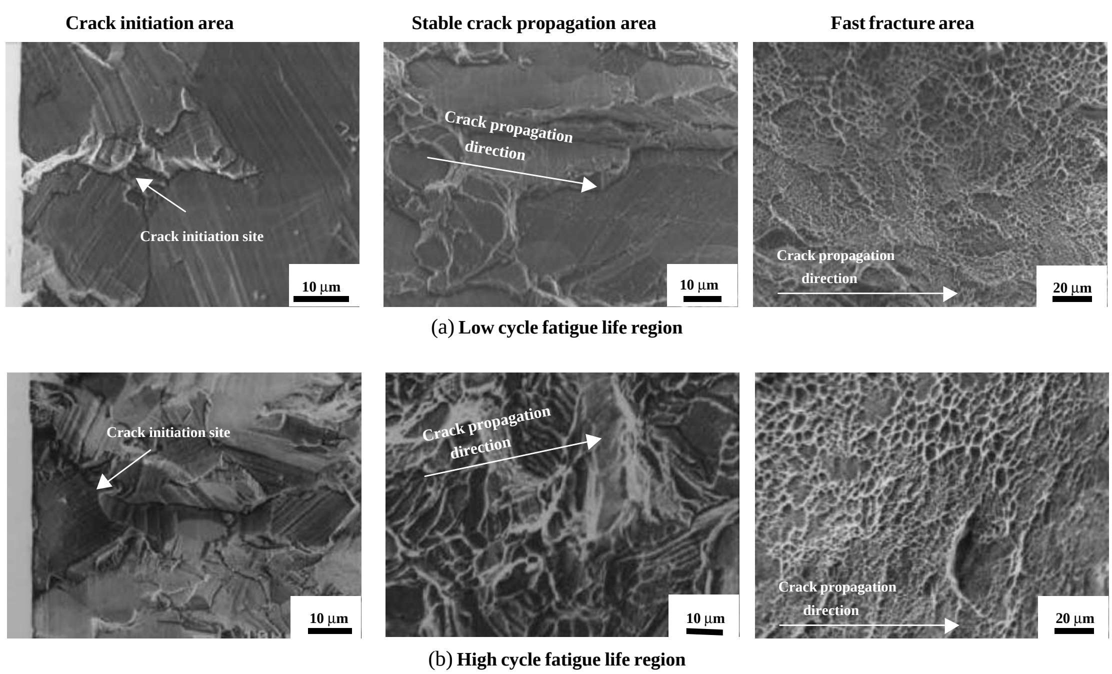

Fig. 13. SEM fractographs of Ti–29Nb–13Ta–4.6Zr aged at 573 K for 259.2 ks after ST tested in: (a) low cycle fatigue life region and (b) high cycle fatigue life region.

case. Relatively wide striations are observed on the stable fracture surface, and equiaxed dimples are observed on the fast fracture surface. These fracture surface morphologies are observed generally ductile metallic materials.

Fig. 13 shows SEM fractographs of STA alloy aged at 573 K in low and high cycle fatigue life regions. The fracture surface in low cycle fatigue life region differs from that of ST alloy, and is relatively flat. Considerable facets are observed near the crack initiation site in both low and high cycle fatigue life regions. In the fast fracture area, a mixed mode fracture surface composed of intergranular and intragranular fractures where fine dimples and flat facets are mixed is observed. This trend in fracture surface was similar to that of STA alloy aged at 593 K. Therefore, the fatigue crack initiation and propagation characteristics of the alloy aged at 593 K was considered to be similar to those in STA alloy aged at 573 K.

Fatigue cracks in STA alloys aged at 573 and 593 K tended to initiate from the subsurface of the specimens especially in high cycle fatigue life region (Fig. 11). The subsurface crack initiation in this study is considered to occur due to slip plane decohesion, which is initiated near the ω phases, because ω phases in β phase are very fine and their volume fraction is relatively large. Therefore, slip cannot move actively in the ω phases or near the ω phases, which leads to the dislocation accumulation near the ω phases. However, further investigation is needed on this point. It is difficult to estimate which stress concentration becomes the crack initiation site, which occurs preferentially near the surface of the specimen or subsurface of the specimen. However, in this study, an obvious change in fatigue life depending on the crack initiation site may not occur.

It has been reported [19] that, as a mechanism of the subsurface crack initiation, when coarse α phases precipitate in β phase, cleavage occurs at {1 0 0} plane of β phase due to the inconsistent slip between {1 1 0 0} plane of α phase and {1 1 0} plane of β phase, especially, in high cycle fatigue life region. Many reports [20–25] have been made on the mechanism of subsurface fatigue crack initiation in β type titanium alloys, but it is difficult to identify the subsurface crack initiation site, and the mechanism of subsurface fatigue crack initiation may change according to the microstructure.

Fig. 14 shows SEM fractographs of STA alloy aged at 673 K in low cycle and high cycle fatigue life regions. The fatigue crack of the present alloy with mixed microstructure of α, β and ω phases mainly initiates from the surface of the specimen in both low and high cycle fatigue life regions. However, a facet is observed near the crack initiation site. The fatigue fracture surface of the alloy aged at 673 K shows slightly more ductile fatigue fracture morphology as compared to other STA alloys because a little striation can be observed on the stable fatigue crack propagation area, which cannot be observed in the other STA alloy, and equiaxed dimples tend to form on the fast fatigue crack propagation area.

Every STA alloy shows more or a little more brittle fracture surface morphology than that of ST alloy. However, the fatigue strength, especially fatigue limit of STA alloy, is more than around two times greater than that of ST alloy. The increase in fatigue strength of STA alloy may be due to the increase in the resistance against small fatigue crack initiation and propagation caused by the precipitation of α and ω phases that leads to the increase in the tensile strength. It has been reported [26] that, for the titanium alloys with relatively fine microstructures, a large part of fatigue life is occupied by the small fatigue crack initiation and propagation life. In the present STA alloys, a fatigue crack was found to initiate due to slip plane decohesion mainly at the surface of the specimen in low cycle fatigue life region, and mainly at the subsurface of the specimen in high cycle fatigue life region. In general, the longer the slip line, the more easily the slip plane decohesion occurs.

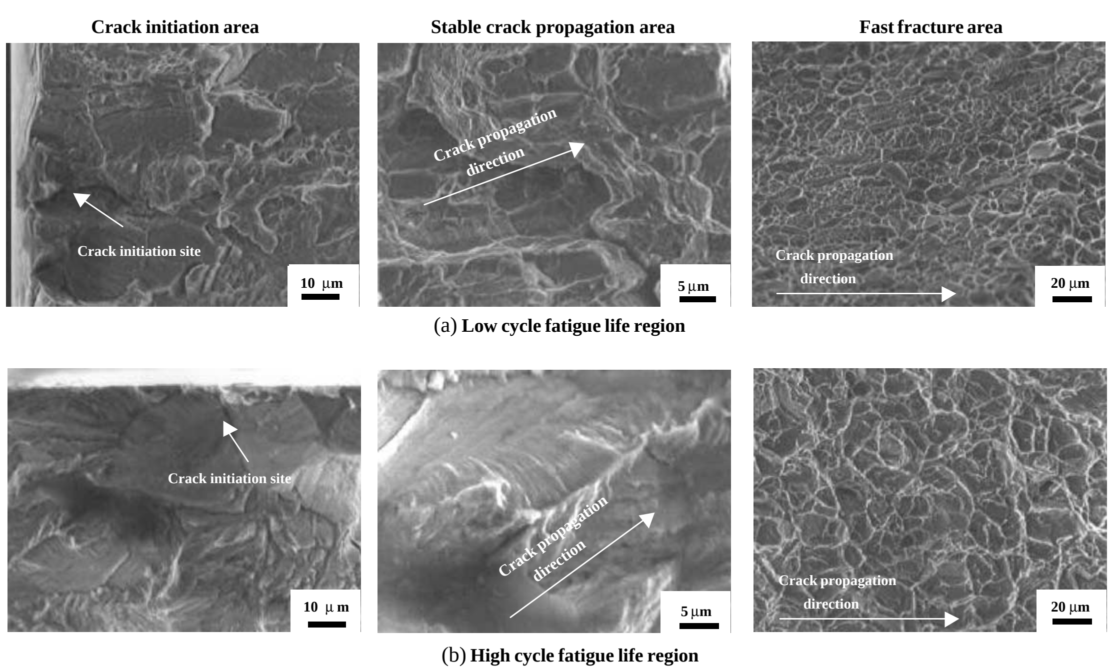

Fig. 14. SEM fractographs of Ti–29Nb–13Ta–4.6Zr aged at 673 K for 259.2 ks after ST tested in: (a) low cycle fatigue life region and (b) high cycle fatigue life region.

When aging is carried out after ST with the present alloy, fine α or ω phase precipitates in β phase with an average diameter of 20 μm, and movement of dislocations is suppressed and length of slip or slip band is decreased. Consequently, the small fatigue crack initiation and propagation are considered to be suppressed.

3.5. Young's modulus

Young's moduli of ST and STA alloys, conventional biomedical $\alpha+\beta$ type Ti–6Al–4V ELI and β type Ti–13Nb–13Zr are shown in Fig. 15. Young's moduli of Ti–6Al–4V and Ti–13Nb–13Zr are quoted from the literature [27,28]. Young's moduli of ST alloy are around 65 GPa, which is much lower than that of Ti–6Al–4V ELI. Young's modulus of STA alloy is greater than that of ST alloy, but still much lower than that of Ti–6Al–4V ELI. Young's modulus of Ti–29Nb–13Ta–4.6Zr is similar to that of Ti–13Nb–13Zr. Young's modulus of Ti–29Nb–13Ta–4.6Zr is found to be controlled by heat treatment.

3.6. Cyto-toxicity

The cyto-toxicity of Ti–29Nb–12Ta–46Zr, Pure Ti and Ti–6Al–4V evaluated by NR and MTT methods are

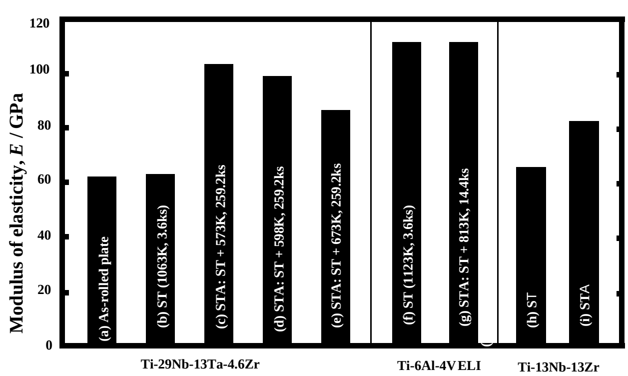

Fig. 15. Comparison of Young's moduli of conventional titanium alloys (Ti–6Al–4V ELI and Ti–13Nb–13Zr) and Ti–29Nb–13Ta–4.6Zr subjected to aging at 573 K, 598 K and 673 K, respectively, for 259.2 ks after ST at 1063 K for 3.6 ks; ST: solution treated, STA: aged after ST.

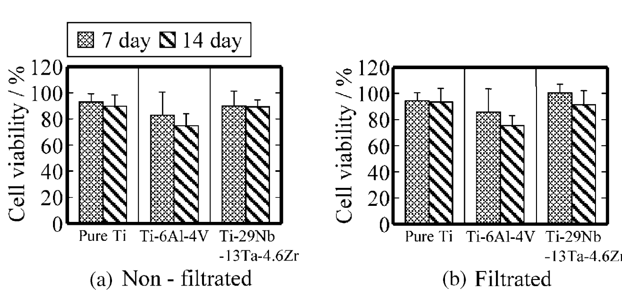

Fig. 16. Cell viability of L-929 in: (a) non-filtrated and (b) filtrated cultivate solutions evaluated by NR method for pure titanium, Ti–6Al–4V and Ti–29Nb–13Ta–4.6Zr.

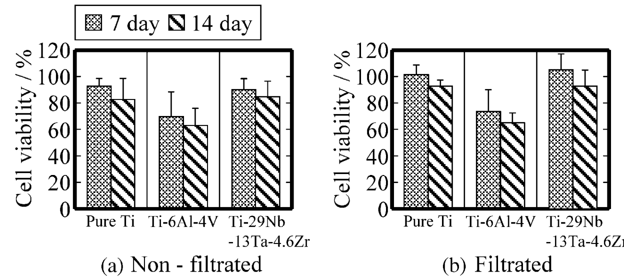

Fig. 17. Cell viability of L-929 in (a) non-filtrated and (b) filtrated cultivate solutions evaluated by MTT method for pure titanium, Ti–6Al–4V and Ti–29Nb–13Ta–4.6Zr.

shown in Figs. 16 and 17, respectively, regardless of the evaluation methods, the cell viability of Ti–29Nb–13Ta–4.6Zr is nearly the same as that of pure Ti and greater than that of conventional biomedical Ti–6Al–4V in both as-extracted and filtrated extracted solutions. Therefore, the biocompatibility of Ti–29Nb–13TA–4.6Zr is judged to be excellent. The trend of cell viability among Ti–29Nb–13Ta–4.6Zr, pure Ti and Ti–6Al–4V is nearly the same regardless of extracted period, although the cell viability of both as-extracted and filtrated extracted solutions decreases with increasing extracted period. However, since the cell viability of filtrated extracted solution is greater than that of as-extracted solution in both NR and MTT methods, not only dissolved metallic ion but also fine debris affects the cyto-toxicity. This fact suggests that it is necessary to suppress the formation of wear as much as possible when metallic materials are used as biomaterial.

4. Conclusions

The fatigue characteristics, Young's modulus and cyto-toxicity of the newly developed β type titanium alloy composed of non-toxic elements such as Nb, Ta and Zr (Ti–29Nb–13Ta–4.6Zr), subjected to ST and various aging treatments after ST, were investigated in relation with microstructures. The following results were obtained:

1. ω phases precipitate in β phase with an average diameter of 20 μm in the Ti–29Nb–13Ta–4.6Zr subjected to aging treatments at 573, 598 and 673 K for 259.2 ks after ST at 1063 K for 3.6 ks. In particular, for the alloy aged at 673 K for 259.2 ks, acicular and bar type α phases precipitate in addition to the ω phases.
2. The fatigue limit of Ti–29Nb–13Ta–4.6Zr aged at 673 K for 259.2 ks after ST at 1063 K for 3.6 ks is the greatest (700 MPa) among other aged alloys due to the precipitation of fine α and ω phases by aging treatment.

3. Striations on the stable fatigue crack propagation area and equiaxed dimples on the fast fatigue crack propagation area are observed in low and high cycle fatigue life regions of Ti–29Nb–13Ta–4.6Zr aged at 673 K for 259.2 ks after ST at 1063 K for 3.6 ks. Therefore, the fatigue fracture surface of Ti–29Nb–13Ta–4.6Zr aged at 673 K for 259.2 ks shows slightly more ductile fracture surface morphology as compared with the alloys aged by other aging methods.
4. Young's modulus of Ti–29Nb–13Ta–4.6Zr is much lower than that of Ti–6Al–4V ELI.
5. Young's modulus of Ti–29Nb–13Ta–4.6Zr can be controlled by aging treatments.
6. Cyto-toxicity of Ti–29Nb–13Ta–4.6Zr is nearly the same as that of pure Ti, and lower than that of Ti–6Al–4V.
7. Based on the data obtained from tensile and fatigue tests, Young's modulus and cyto-toxicity in this study, Ti–29Nb–13Ta–4.6Zr is proposed as a very useful biomaterials.

Acknowledgements

Some parts of this study were supported by NEDO (New Energy and Industrial Technology Development Organization, Tokyo, Japan), Grant-in-Aid for Promoting Scientific Frontier Research from Ministry Education, Science and Culture (Tokyo, Japan), Grant-in-Aid for Scientific Research from Japan Society for Promotion of Science (Tokyo, Japan), Mitsubishi Foundation (Tokyo, Japan), Kotai Foundation (Toyohashi, Japan), The Iron and Steel Institute of Japan (Tokyo, Japan), The Light Metal Education Foundation (Osaka, Japan), and Suzuki Foundation (Hamamatsu, Japan).

References

[1] ASTM designation F2066-01. Standard specification for wrought titanium-15 molybdenum alloy for surgical implant applications. Philadelphia, PA: ASTM, 2001, p. 1605–8.

[2] ASTM designation draft #3. Standard specification for wrought taitanium-35Niobium-7zirconium-5tantalum alloy for surgical implant applications (UNS R58350). Philadelphia, PA: ASTM, 2000.

[3] ASTM designation draft #6. Standard specification for wrought titanium-3aluminun-2.5vanadium alloy seamless tubing for surgical implant applications (UNS R56320). Philadelphia, PA: ASTM, 2000.

[4] Davidson JA, Georgette FS. State of the art materials for orthopedic prosthetic devices. Proceedings of the implant manufacturing and material technology. Society of Manufacturing Engineers. Dearborn, 1987: EM87-122-1-EM87-122-26.

[5] Niinomi M. Recent metallic materials for biomedical applications. Metal Mater Trans A 2002;33A:477–86.

[6] Kuroda D, Niinomi M, Morinaga M, Kato Y, Yashiro T. Design and mechanical properties of new β type titanium alloys for implant materials. Mat Sci Eng A 1998;A243:244–9.

[7] Niinomi M, Kuroda D, Fukunaga K, Morinaga M, Kato Y, Yashiro T, Suzuki A. Corrosion wear fracture of new β type biomedical titanium alloys. Mat Sci Eng A 1999;A263: 193–9.

[8] Kuroda D, Niinomi M, Fukui H, Suzuki A, Hasegawa S. Mechanical performance of newly developed β-type titanium alloy, Ti–29Nb–13Ta–4.6Zr, for biomedical applications. In: Niinomi M, Okabe T, Taleff EM, Lesure DR, Lippard HE, editors. Structural biomaterials for the 21st century. Warrendale: TMS, 2001. p. 99–106.

[9] Akahori T, Niinomi M, Yabunaka T, Kuroda D, Fukui H, Suzuki A, Hasegawa J. Fretting fatigue characteristics of biomedical new β titanium alloy, Ti–29Nb–13Ta–4.6Zr. In: Hanada S, Zhong Z, Nam SW, Wright RN, editors. Proceedings of the PRICM 4: The Jpn. Inst. Metals, 2001. p. 209–12.

[10] Steinemann SG. Corrosion of surgical implants—in vivo and in vitro tests. In: Winter GD, Leray JL, de Groot K, editors. Evaluation of biomaterials. New York: Wiley, 1980. p. 1–34.

[11] Kawahara H, Ochi S, Tanetani K, Kato K, Isogai M, Mizuno Y, Yamamoto H, Yamaguchi A. Biological test of dental materials, Effect of pure metals upon the mouse subcutaneous fibroblast, strain L cell in tissue culture. J Jpn Soc Dent Apparat Mater 1963;4:65–75.

[12] Kudo S, Ozawa M. Application of piezoelectric composite-bar method to elastic modulus measurement of ceramics (part 1). J Ceramics Soc Japan 1990;98:635–57.

[13] Borenfreund E, Purener JA. Toxicity determined in vitro by morphological alternations and neutral red absorption. Toxicl Lett 1985;24:119–24.

[14] Mosman T. Rapid colorimetric assay for cellular growth and survival, Application to proliferation and cytotoxicity assay. J Immunol Methods 1983;65:55–63.

[15] Jha SK, Ravichandran KS. Effect of mean stress (stress ratio) and aging on fatigue crack growth in a metastable beta titanium Ti–10V–2Fe–3Al. Metal Mater Trans A 2000;37A: 703–14.

[16] Okazaki M, Hizume T. Effect of microstructure on small fatigue crack growth and the crack opening—closing behavior in Ti–6Al–4V alloy. J Soc Mater Sci Japan 1994;43:1238–44.

[17] Akahori T, Niinomi M, Fukunaga K, Inagaki I. An investigation of the effect of fatigue deformation on the residual properties of Ti–6Al–4V ELI. Metall Mater Trans A 2000;31A:1937–48.

[18] Akahori T, Niinomi M, Fukunaga K, Inagaki I. Effects of microstructure on the short fatigue crack initiation and propagation characteristics of biomedical alpha/beta titanium alloys. Metall Mater Trans A 2000;31A:1949–58.

[19] Ruppen J, Bhowal P, Eylon D, Macevily AJ. On the process of subsurface fatigue crack initiation in Ti–6Al–4V. ASTM STP 1979;675:47–68.

[20] Lindemann J, Wagner L. Mean stress sensitivity in fatigue of alpha, alpha + beta and beta titanium alloys. Mater Sci Eng A 1997;A234–236:1118–21.

[21] Yokoyama H, Umezawa K, Nagai K, Suzuki T. Distribution of internal crack initiation sites in high-cycle fatigue for titanium alloys. ISIJ 1997;37:1237–44.

[22] Chunbian J, Tokaji K, Nakashima M, Ogawa T. Effect of microstructure on fatigue behavior of Ti–15Mo–5Zr–3Al alloy. J Soc Mat Sci Japan 1995;44:933–8.

[23] Tokaji K, Ohya K, Kariya H. Effect of grain size on fatigue strength and substructure crack initiation in beta Ti–22V–4Al alloy. J Soc Mat Sci Japan 2000;49:994–1001.

[24] Shiozawa K, Kuroda Y, Nishino S. Effect of stress ration subsurface fatigue crack initiation behavior of beta-type titanium alloy. J Jpn Soc Mech Eng A 1998;64:94–101.
[25] Shankar PS, Ravichandran KS. Fatigue response and micro-mechanism of crack initiation in Ti–10V–2Fe–3Al titanium alloy. In: Boyer RR, Eylon D, Lütjering G, editors. Fatigue behavior of titanium alloys. Warrendale: TMS, 1998. p. 135–47.
[26] Hagiwara M. Mechanism of Fatigue of titanium alloys. Mater Jpn 1998;37:35–8.
[27] Welsch G, Bunk W. Deformation modes of the α-phase of Ti–6Al–4V as a function of oxygen concentration and aging temperature. Metal Trans A 1982;13A:889.
[28] Mishra AK, Davidson JA, Poggie RA, Kovacs P, FizGerald TJ. Mechanical and tribological properties and biocompatibility of diffusion hardened Ti–13Nb–13Zr—A new titanium alloy for surgical implants. In: Brown SA, Lemons JE, editors. Medical applications of titanium and its alloys. West Conshohocken: ASTM, 1996 STP 1272: p. 96–113.